KIC 10417986: Spectroscopic Confirmation of the Nature of the Binary System with a δ Scuti Component

Guo-Jie Feng[1,2], Ali Esamdin[1,2], Jian-Ning Fu[3], Hu-Biao Niu[1], Peng Zong[3], Tao-Zhi Yang[4], Shu-Guo Ma[1,2], Jing Xu[1], Chun-Hai Bai[1], Yong Wang[1], Wei-Chao Sun[1], and Xin-Liang Wang[1]

[1] Xinjiang Astronomical Observatory, Chinese Academy of Sciences, Urumqi, Xinjiang 830011, China; aliyi@xao.ac.cn
[2] University of Chinese Academy of Sciences, Beijing 100049, China
[3] Department of Astronomy, Beijing Normal University, Beijing 100875, China; jnfu@bnu.edu.cn
[4] Ministry of Education Key Laboratory for Nonequilibrium Synthesis and Modulation of Condensed Matter, School of Physics, Xi'an Jiaotong University, 710049 Xi'an, China

Abstract

KIC 10417986 is a short orbital period (0.0737 day) ellipsoidal variable star with a δ Sct and γ Dor hybrid pulsation component discovered by Kepler. The ground-based spectroscopic observations were carried out in the winters of 2020 and 2021 to investigate the binary nature of this star. We derive the orbital parameters using the rvfit code with a result of $K_1 = 29.7 \pm 1.5 \, \mathrm{km \, s^{-1}}$, $\gamma = -18.7 \pm 1.7 \, \mathrm{km \, s^{-1}}$, and confirm an orbital period of 0.84495 day instead of the result given by Kepler. The atmospheric parameters of the primary are determined by the synthetic spectral fitting technique with the estimated values of $T_{\mathrm{eff}} = 7411 \pm 187$ K, log $g = 4.2 \pm 0.3$ dex, [M/H] $= 0.08 \pm 0.09$ dex and $v\sin i = 52 \pm 11 \, \mathrm{km \, s^{-1}}$. KIC 10417986 is a circular orbit binary system. From the single-lined nature and mass function of the star, the derived orbital inclination is $26° \pm 6°$, and the mass of the secondary is $0.52^{+0.18}_{-0.09} \, M_{\odot}$, which should be a late-K to early-M type star. Fourteen frequencies are extracted from Kepler light curves, of which six independent frequencies in the high-frequency region are identified as the p-mode pulsations of δ Sct star, and one independent frequency in the low-frequency region ($f_2 = 1.3033 \, \mathrm{cd^{-1}}$) is probably the rotational frequency due to the starspots rather than the ellipsoidal effect.

Key words: techniques: spectroscopic – (stars:) binaries: spectroscopic – stars: individual (KIC 10417986) – stars: oscillations (including pulsations) – stars: variables: delta Scuti – (stars:) starspots

1. Introduction

The study of binary stars, especially eclipsing binaries, has gained a new perspective since the beginning of the CoRoT, Kepler and TESS space missions (Damiani et al. 2010; Uytterhoeven et al. 2011; Maceroni et al. 2013; Barros et al. 2016; Mortensen et al. 2021). The high-precision photometric data from space, combined with ground-based spectroscopic data, allow a precise determination of stellar properties, such as mass, radius and luminosity (e.g., Guo et al. 2016; Chen et al. 2019; Liakos 2020; Chen et al. 2020). In particular, by studying pulsating components in eclipsing binary systems, such as the δ Sct and γ Dor variables, one can build appropriate asteroseismic models based on the precise stellar parameters to constrain the stellar structure and evolution. However, in the case of non-eclipsing binary systems, the two stars do not eclipse each other in the direction of our sight line. Especially for single-line spectroscopic binaries, whose mass ratio cannot be determined (Videla et al. 2022), this lack of information will limit the method of detailed asteroseismic modeling of the pulsating components.

δ Sct are stars located in what is known as the instability strip, on or a little above the main sequence in the Hertzsprung–Russell (H-R) diagram (Breger 2000). They are late-A to early-F spectral type stars with masses between 1.5 and 2.5 $M_{\odot}$, and luminosities in the range $0.6 \leqslant \log(L/L_{\odot}) \leqslant 2.0$. These stars typically pulsate in radial and low-order non-radial modes, belong to p-mode pulsations with amplitudes less than 0.3 mag, and pulsation periods ranging from 15 minutes up to 8 hr (Rodríguez & Breger 2001; Uytterhoeven et al. 2011). The oscillations of those stars are self-excited through the κ mechanism that occurs in the partial ionization zone of He II (Li & Stix 1994; Gautschy & Saio 1995; Breger 2000; Handler 2009; Balona et al. 2015). They also pulsate in high-order non-radial modes, which may be due to turbulent pressure in the hydrogen convective zone (Antoci et al. 2014).

KIC 10417986 = HD 187276 ($K_p = 9.13$ mag, $\alpha_{J2000} = 19^{\mathrm{h}}46^{\mathrm{m}}59^{\mathrm{s}}.70$, $\delta_{J2000} = +47°32'37''.71$) was identified as a binary star with a very short orbital period of 0.0737(1) days and suggested to be a possible triple system (Conroy et al. 2014; Kirk et al. 2016). Then Gaulme & Guzik (2019) flagged it as an ellipsoidal variable star with δ Sct and γ Dor hybrid pulsations by applying a data inspection tool (DIT) to the whole Kepler light curve. Based on known parameters from

Table 1
Table of Stellar Parameters from Catalogs for KIC 10417986

Parameter	The Spitzer Kepler Survey Catalog (Werner et al. 2021)	TESS Input Catalog (Stassun et al. 2019)	Gaia DR2 (Gaia Collaboration et al. 2018)
ID	KIC 10417986	TIC 272599738	2086579087597378816
$T_{\rm eff}$ (K)	7430 ± 324	7808 ± 143	7484
log g (dex)	4.218 ± 0.210	4.1539 ± 0.0751	
[Fe/H] (dex)	0.07 ± 0.35		
Mass ($M_\odot$)	1.581 ± 0.214	1.853 ± 0.291	
Radius ($R_\odot$)	$1.619^{+0.575}_{-0.230}$	1.888 ± 0.053	1.95
Parallax (mas)			4.1128 ± 0.0302
Distance (pc)		241.4630 ± 1.7760	$241.4635^{+1.7886}_{-1.7631}$
Luminosity ($L_\odot$)		11.93847 ± 0.47378	$10.774^{+0.127}_{-0.126}$

Kepler and Gaia catalogs (see Table 1), the primary component is a late-A or early-F spectral type star.

KIC 10417986, as an example for astronomical research at Chiang Rai Rajabhat University, was studied for the first time by Aindang et al. (2021), who derived the absolute parameters of two components under the assumption that the system is a contact binary system whose components are main sequence stars. They found that the system might have a high mass transfer rate from the primary component onto the secondary one. However, this study was based on the light curves of Kepler and TESS online archives without spectral data, and no detailed study of the system was possible. In this paper, we carry out a more detailed study of KIC 10417986 based on the Kepler photometric data and the ground-based spectroscopic data, which are described in Section 2. The orbital parameters, atmospheric parameters and frequency analysis are presented in Section 3. We provide a brief discussion on the probable rotation frequency f_2, orbital inclination, the mass of the secondary and the age of the system in Section 4. The summary of this work is given in Section 5.

2. Kepler Photometric Data and Ground-based Spectroscopic Data

2.1. Kepler Photometric Data

KIC 10417986 was observed by NASA space mission Kepler from BJD 2454953.54 to 2456424.00, including fifteen quarters (Q0–Q6, Q8–Q10, Q12–Q14 and Q16–Q17) of long cadence (LC) data with 29.4 minute sampling and one quarter (Q2.1, Q2.2, and Q2.3) of short cadence (SC) data with 58.8 s sampling (Prša et al. 2011; Slawson et al. 2011; Kirk et al. 2016). This star's target pixel files (TPFs) were downloaded from the Mikulski Archive for Space Telescopes (MAST[5]), and the Lightkurve package (Vinícius et al. 2018; Dotson et al. 2019; Barentsen et al. 2021) was adopted to extract light curves from the TPFs. A series of different apertures of pixel sizes was

tested on TPFs to optimize the photometry. After extracting the light curves, we detrended and normalized the flux by a linear or polynomial fitting. Then, we converted the corrected flux to magnitude. Finally, a total of 50168 LC data points and 123255 SC data points was obtained after removing outliers by sigma clipping. Both LC and SC light curves are depicted in Figure 1. It can be seen that the period of the maximum amplitude is close to 0.04 days, and the mean amplitude (∼0.6 mmag) of the SC light curve is larger than that (∼0.3 mmag) of the LC light curve because the high-frequency amplitude of LC data is suppressed by the long exposure time (Yang et al. 2018).

2.2. Ground-based Spectroscopic Data

The spectroscopic observations for KIC 10417986 aimed to derive the radial velocities (RVs) of the components. As a first step, we have gathered 16 echelle spectra with the Beijing Faint Object Spectrograph and Camera (BFOSC) attached to the 2.16 m telescope at the Xinglong Station of National Astronomical Observatories, Chinese Academy of Sciences (NAOC) on 2020 October 4 and 5. We chose the combination of echelle and grism E9+G11 with the slit size of 1″.6, which provided a resolution of ∼0.55 Å pixel^{-1} and a wavelength coverage from 3900 to 9000 Å (Fan et al. 2016). Eight spectra per night were taken with the goal to cover the possible orbital period of 0.0737 days (≈2 hr) suggested by Kirk et al. (2016). The exposure time for each spectrum was 15 minutes with a temporal resolution ∼12.5% of the orbital period. However, the result showed that the RVs do not change periodically for 2 hr in the two-hour observation every night, and the difference in RVs between the two days is about 30 km s^{-1}.

For solving this system, supplemental spectroscopic observations were performed with the BFOSC instrument of the 2.16 m telescope at the Xinglong Station of NAOC, and the Nanshan Echelle Spectrograph (NES) instrument of the 1.2 m telescope at the Nanshan Station of Xinjiang Astronomical Observatory (XAO) in the winter of 2021. The NES is a fiber-fed moderate- and low-resolution echelle spectrograph with
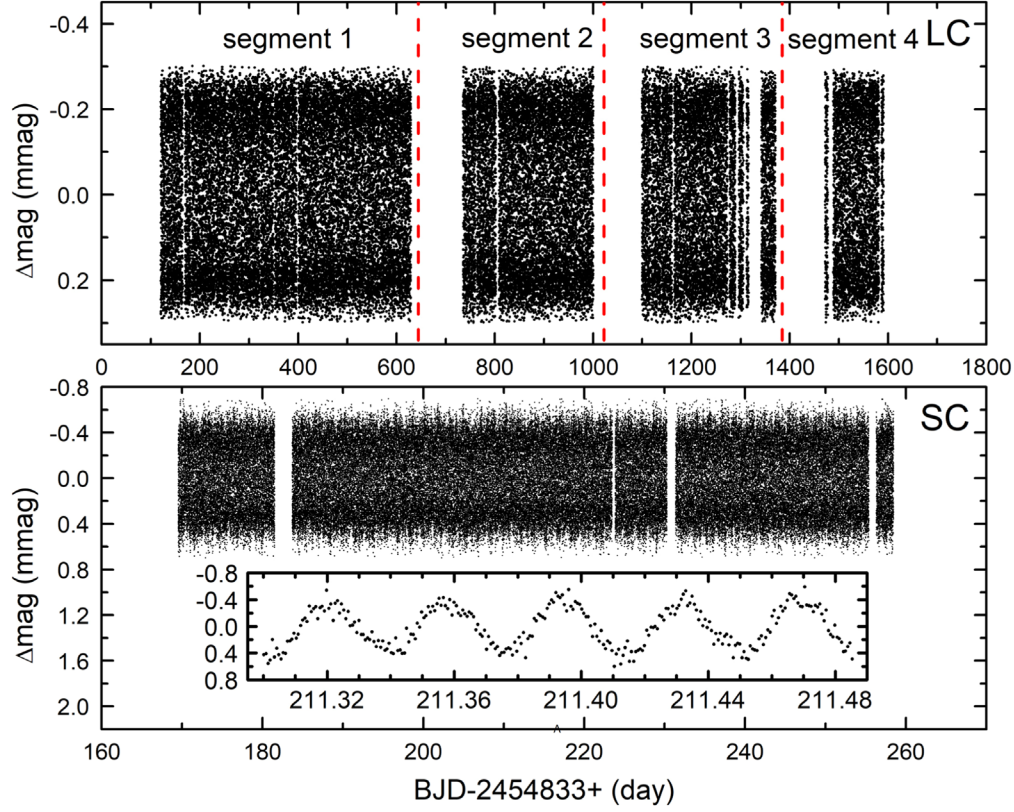

Figure 1. Detrended Kepler LC (top) and SC (bottom) light curves of KIC 10417986. The inset of SC features the zoomed area covering 0.185 days of observations to visualize the photometric variability.

2″4 aperture fiber, which has been developed by Astronomical Consultants & Equipment, Inc. (ACE). The NES instrument using the low-resolution grating (95 grooves mm^{-1}) and moderate-resolution grating (79 grooves mm^{-1}) was employed for the observations. The low-resolution grating provided a spectral coverage from 3680 to 10,290 Å while the resolution of the spectra is from 0.13 to 0.35 Å pixel^{-1}, and the moderate-resolution grating provided a spectral coverage from 3770 to 10,040 Å while the resolution of the spectra is from 0.069 to 0.178 Å pixel^{-1}. The observations were carried out using the BFOSC (E9+G11+slit1″6) on October 20, the NES (low-resolution) on November 24, the NES (moderate-resolution) on November 25 and the NES (moderate-resolution) with 2×2 on-chip binning on November 29. A total of eleven spectra were obtained during this observation run.

High-resolution spectroscopic observations for KIC 10417986 were also carried out with the fiber-fed High-Resolution Spectrograph (HRS) (Fan et al. 2016) instrument attached to the 2.16 m telescope at the Xinglong Station, NAOC on 2022 March 26. The spectrograph is equipped with a back-illuminated red-sensitive 4096×4096 E2V CCD-203-82

with a pixel size of 12 μm. This set-up provides a resolution of ~0.025 Å pixel^{-1} corresponding to a 2″4 aperture fiber and a spectral coverage range from 3600 to 10,000 Å. We collected two high-resolution spectra with an exposure time of 30 minutes. The signal-to-noise ratio (S/N) is about 26 for each spectrum.

A detailed journal of all spectroscopic observations for KIC 10417986 is given in Table 2, and a total of 29 spectra is obtained. First, the spectra were reduced by the IRAF/CCDRED package with bias subtraction, trimming and flat-field correction. Then, we used the STSDAS/lacos_spec package (van Dokkum 2001) to remove the cosmic rays. Finally, the extraction and normalization of spectra were done utilizing the IRAF/ECHELLE package. Meanwhile, wavelength calibration was performed using the Fe-Ar or Th-Ar lamp taken during the same observation night.

Considering the limit of resolution and S/N of our spectra, we did not find any clue of spectral lines belonging to the secondary component of KIC 10417986. This indicates that the luminosity of the secondary is much lower than that of the primary.

Table 2
Journal of Spectroscopic Observations for KIC 10417986

Date	Observatory	Telescope	Instrument	Spectra	Exposure Time	S/N
2020 Oct. 4	NAOC	2.16 m	BFOSC (E9+G11+slit1″6)	8	15 minutes	340
2020 Oct. 5	NAOC	2.16 m	BFOSC (E9+G11+slit1″6)	8	15 minutes	150
2021 Oct. 20	NAOC	2.16 m	BFOSC (E9+G11+slit1″6)	2	30 minutes	710
2021 Nov. 24	XAO	1.2 m	NES (low-resolution)	3	30 minutes	39
2021 Nov. 25	XAO	1.2 m	NES (moderate-resolution)	3	60 minutes	17
2021 Nov. 29	XAO	1.2 m	NES (moderate-resolution)	3	60 minutes	48
2022 Mar. 26	NAOC	2.16 m	HRS	2	30 minutes	26

3. Analysis

3.1. Determination of the Spectroscopic Orbital Solution

In order to extract the RVs of KIC 10417986 from the reduced spectra, the following formula is used

$$\mathrm{RV} = C \times \frac{\Delta\lambda}{\lambda}, \tag{1}$$

where C is the speed of light in a vacuum, λ is the standard center wavelength of the spectral absorption line and $\Delta\lambda$ is the center wavelength difference between the object and the RV standard stars for the same absorption line. For KIC 10417986, we can only measure the RVs of the primary limited by the spectrograph resolution and luminosity difference between the primary and secondary stars. First, we measure the center positions of the Balmer lines (H_α, H_β, H_γ and H_δ) by using a Gaussian fit. Then, the calibration of the RVs is performed with the RV standard star HR 328 or HIP 087998 observed during the same night. Finally, the heliocentric velocity is calculated by using the IRAF/RVSAO/*bcvcorr* package to correct the motion of Earth. The mean values of the derived RVs from our spectra are listed in Table 3.

We subsequently determine the orbital parameters of KIC 10417986 by using the rvfit[6] code (Iglesias-Marzoa et al. 2015), which implements the Adaptive Simulated Annealing (ASA) global minimization method to fit RVs of binaries. In the beginning, we set the orbit period P, the time of periastron passage T_p, the orbital eccentricity e, the argument of periastron ω, the systemic RV γ and the RV amplitude K_1 of the primary as free parameters in the first run. The results show a very small value of eccentricity e, indicating a circular orbit. So, we fix the eccentricity e to zero and ω to 90°.0 in the second run. The same results are fitted to the rest of the parameters. The orbital phases are listed in the second column of Table 3. The adjusted and derived orbital parameters are listed in Table 4, and the uncertainties are obtained with Markov Chain Monte Carlo (MCMC) analysis.

The fitted RV curve compared with the RV measurements of the primary is plotted in Figure 2. The red solid line in the top

---

Table 3
Measured RVs for the Primary of KIC 10417986

HJD (2459000+)	Orbital Phase	RV (km s^{-1})	RV Error (km s^{-1})
126.98428	0.775 90	6.2	5.9
126.99476	0.788 30	8.5	7.7
127.00523	0.800 70	4.8	6.4
127.01570	0.813 09	5.6	6.6
127.02618	0.825 49	0.3	6.9
127.03665	0.837 88	−1.0	6.1
127.04712	0.850 28	−2.9	5.0
127.05760	0.862 67	0.6	5.8
128.03107	0.014 78	−24.3	4.1
128.04154	0.027 18	−19.0	6.0
128.05202	0.039 57	−27.5	5.2
128.06249	0.051 97	−26.9	7.2
128.07296	0.064 36	−29.6	1.6
128.08344	0.076 76	−32.7	5.0
128.09391	0.089 16	−28.5	6.4
128.10439	0.101 55	−30.3	5.6
508.04467	0.761 63	11.9	2.5
508.06559	0.786 38	13.3	2.0
543.03243	0.169 71	−47.6	7.6
543.05401	0.195 26	−51.8	3.7
543.09270	0.241 05	−54.9	12.0
544.02667	0.346 40	−47.5	6.9
544.08042	0.410 01	−34.5	11.3
544.12251	0.459 83	−21.3	8.4
548.04498	0.102 07	−41.4	10.5
548.08786	0.152 82	−45.0	8.1
548.12972	0.202 37	−45.5	3.2
665.33057	0.909 80	−3.0	2.9
665.35296	0.936 31	−6.2	5.0

panel represents the best-fitting with an orbital period of $P = 0.84495$ day, velocity variation amplitude of $K_1 = 29.7$ km s^{-1} and the systemic RV of $\gamma = -18.7$ km s^{-1}. The bottom panel displays the residuals of the best-fitting.

Based on the fact that the flux we observed is mainly from the primary component, the luminosity ($L = 10.774$ $L_\odot$) provided by Gaia is approximately that of the primary. By the revised mass–luminosity relation (Eker et al. 2015), the mass of the primary component is estimated to be $M_1 = 1.73(3)$ $M_\odot$. From the mass function, we have derived all possible
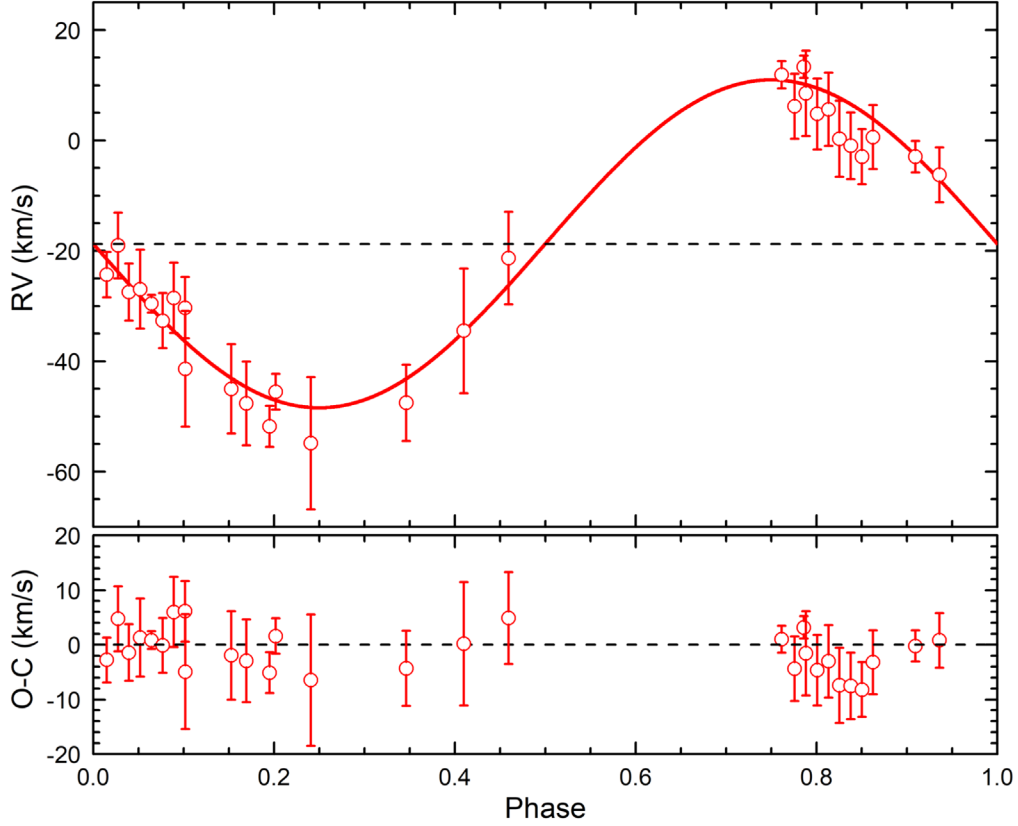
Figure 2. Top panel: The phase diagram of RVs for the primary of KIC 10417986 with the observed RVs (red open circles) and the orbital fitting (red solid lines). Bottom panel: residuals with uncertainties.

Table 4
Orbital Parameters of KIC 10417986

Parameter	Value
Adjusted Quantities	
P (d)	0.84495 ± 0.00002
T_p (HJD)	2459126.3287 ± 0.0095
e^{a}	0.0
ω^a (deg)	90.0
γ (km s^{-1})	-18.7 ± 1.7
K_1 (km s^{-1})	29.7 ± 1.5
Derived Quantities	
$a_1 \sin i$ ($R_\odot$)	0.50 ± 0.02
$f(m_1, m_2)$ ($M_\odot$)	0.0023 ± 0.0003
Other Quantities	
χ^2	16.799296
N_{obs} (primary)	29
Time span (days)	538.36868
rms$_1$ (km s^{-1})	4.2

Note.
[a] Parameter fixed beforehand.

combinations between the orbital inclination (i) and the mass of the secondary (M_2) shown in Figure 3. For $i < 15°$ ($L_2 > 1\,L_\odot$), a double-lined spectroscopic binary would have been found. All other solutions result in a low-mass companion star. Moreover, the orbital inclination i_{orb} cannot reach high values, since there are no eclipses seen in the light curves of KIC 10417986 (see Section 3.3). See Section 4 for a detailed discussion.

3.2. Determination of the Atmospheric Parameters

We derive the atmospheric parameters (i.e., effective temperature T_{eff}, surface gravity log g, metallicity [M/H] and rotation velocity $v$sin$i$) using the synthetic spectral fitting technique provided by the code iSpec (Blanco-Cuaresma et al. 2014; Blanco-Cuaresma 2019). The synthetic spectra are calculated with the radial transfer code SPECTRUM (Gray & Corbally 1994), the Castelli grids of the plane-parallel ATLAS9 model atmospheres (3500 K $\leqslant T_{\text{eff}} \leqslant$ 8750 K, 0.0 dex $\leqslant$ log $g \leqslant$ 5.0 dex, and -5.00 dex $\leqslant$ [M/H] $\leqslant$ 1.00 dex) (Kurucz 2005), the solar abundance of Grevesse & Sauval (1998), and the Vienna Atomic Line Database (VALD; Piskunov et al. 1995) line list.
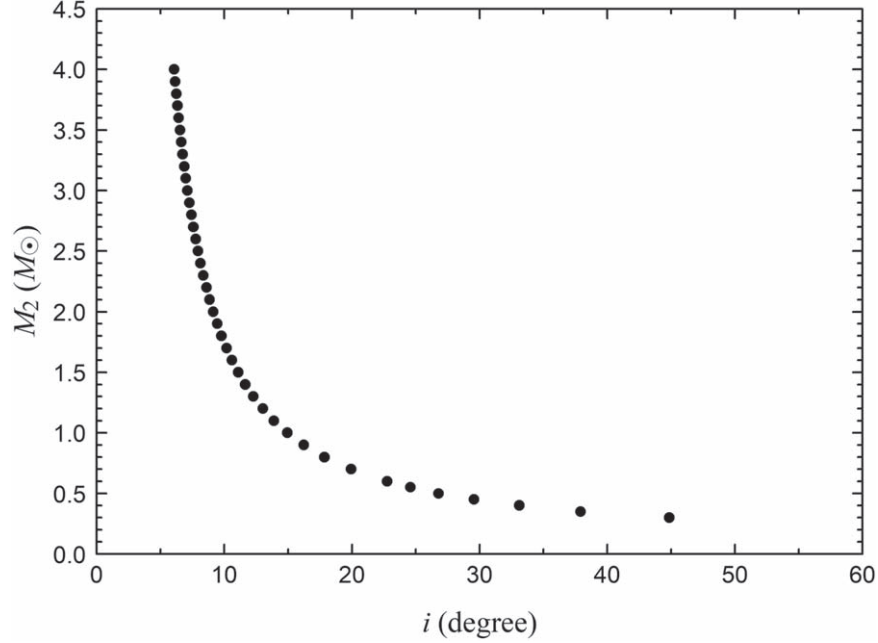
Figure 3. Possible combinations between the orbital inclination (i) and the mass of secondary (M_2) from the mass function.

To improve the S/N, we combine the spectra after correcting the RV on the same observation night (except for the data on 2021 November 25, because of the very low S/N), with wavelengths from 480 to 650 Å for HRS, 450 to 650 Å for NES (moderate-resolution) and 450 to 750 Å for NES (low-resolution). Then we clean the regions of the spectra that may be affected by telluric lines, and degrade the resolution to 80,000 and 18,000 for HRS and NES, respectively. Finally, we use three combined higher resolution spectra and 18 BFOSC lower resolution spectra to derive the atmospheric parameters.

In the iteration process, we set the effective temperature T_{eff}, surface gravity log g, metallicity [M/H], microturbulence velocity v_{mic}, rotation velocity $v\sin i$ and resolution R as the free parameters, and use the parameters given by the Spitzer Kepler Survey catalog (Werner et al. 2021) (see Table 1) as the initial values of T_{eff}, log g and [M/H]. The macro-turbulence velocity v_{mac} follows an empirical relation of Sheminova (2019), and the limb darkening coefficient is fixed to be 0.6 (Hestroffer & Magnan 1998; Blanco-Cuaresma 2019; Sarmento et al. 2020). We finally obtain 21 sets of atmospheric parameters by comparing the calculated spectra to the observed spectra. The values of $T_{eff} = 7411 \pm 187$ K and log $g = 4.2 \pm 0.3$ dex are their corresponding mean values derived from the 21 spectra. The values of [M/H] $= 0.08 \pm 0.09$ dex and $v\sin i = 52 \pm 11$ km s^{-1} are mean values derived from three combined higher resolution spectra, as they cannot be determined with high precision from the lower resolution spectra. The parts of the spectral fitting to HRS, NES (moderate-resolution), NES

(low-resolution) and BFOSC are depicted from the top to bottom panels in Figure 4, respectively.

3.3. Fourier Analysis

The Fourier analysis is performed with the software Period04 v.1.2.0 (Lenz & Breger 2005) to LC and SC data of KIC 10417986. A multi-frequency non-linear least-squares fit is used to extract significant frequencies of each light curve with the equation

$$\Delta m = \sum_i A_i \sin[2\pi(f_i t + \phi_i)], \qquad (2)$$

where A_i is the amplitude, f_i is the frequency and ϕ_i is the phase. We search for significant peaks up to the LC and SC Nyquist frequencies (24.5 cd^{-1} and 734 cd^{-1}, respectively) in the first run, but no peaks are found beyond the frequency of 50 cd^{-1} in SC data. So, we limit the lower and upper bound of the frequency to 0 and 50 cd^{-1} for both LC and SC data, and a standard pre-whitening procedure (Zong et al. 2019) is performed to subtract frequencies from light curves until a 5.6σ limit (5.6σ meaning the risk of a false detection is less than 1/10,000, recommended by Zong et al. 2016). The Nyquist alias frequencies in LC data are identified by cross-matching with the frequencies in SC data (Murphy et al. 2013).

A total of 14 and 10 significant frequencies are detected from LC and SC light curves of KIC 10417986, respectively. The frequency values of LC and SC data with respective amplitude and S/N are listed in Table 5. The corresponding uncertainties of frequencies and amplitudes are derived by using the Monte
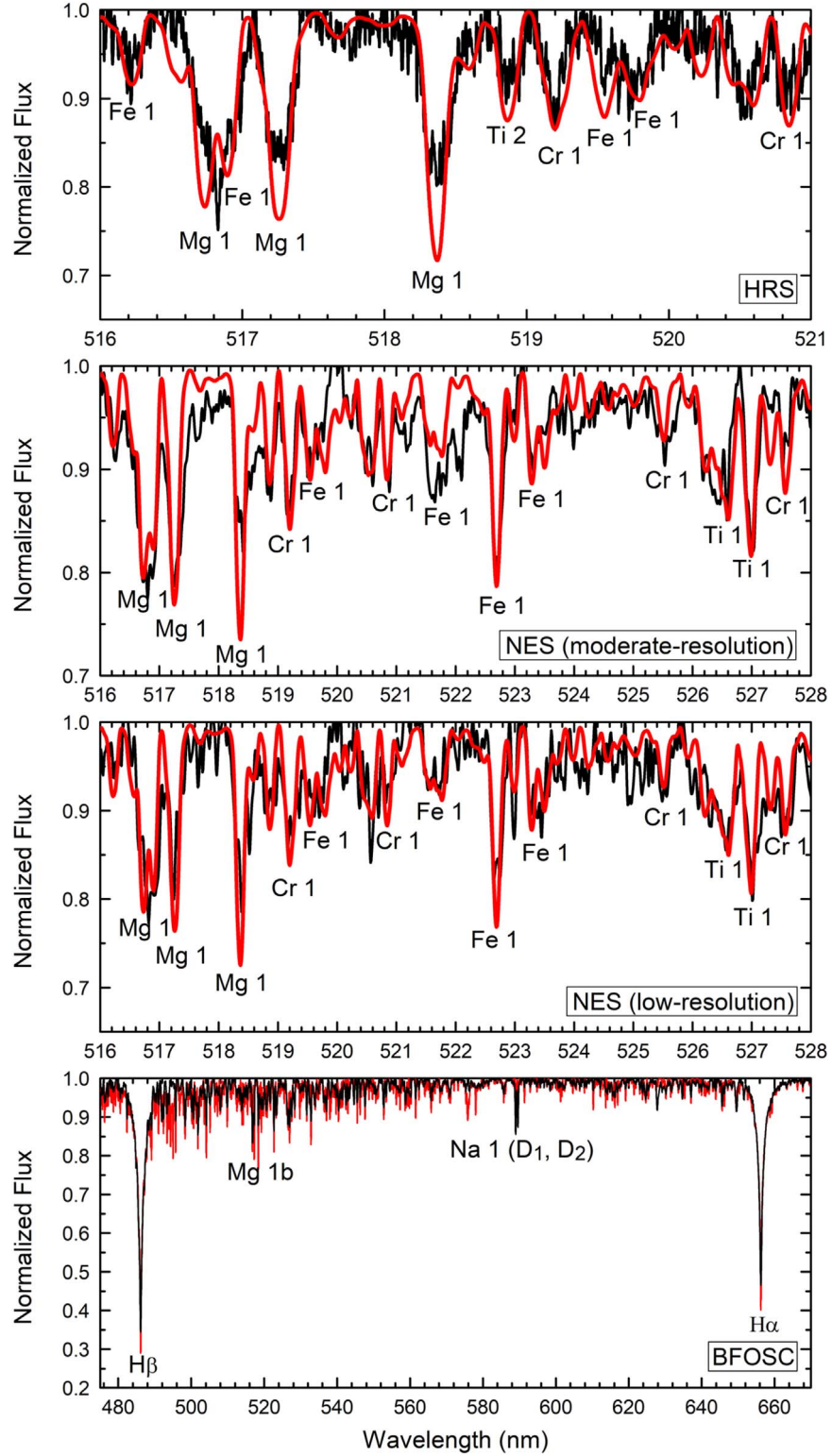
Figure 4. Comparisons of the fitted spectra (red line) and the observed spectra of KIC 10417986 (black line). The parts of the spectra observed by HRS, NES (moderate-resolution), NES (low-resolution) and BFOSC are shown from the top to bottom panels, respectively.

Table 5
List of Frequencies Detected from LC and SC Data of KIC 10417986

ID	Frequency (LC) (cd^{-1})	Amplitude (LC) (mmag)	S/N (LC)	Frequency (SC) (cd^{-1})	Amplitude (SC) (mmag)	S/N (SC)	P_{pul}/P_{orb}	Comment
f_1	27.125672(3)	0.230(3)	1180.1	27.125 68(2)	0.407(2)	734.8	0.044	p-mode
f_2	1.303334(8)	0.0247(5)	75.8	1.3038(1)	0.0303(6)	30.6	⋯	rotation?
f_3	26.532997(9)	0.0179(4)	94.0	26.5329(1)	0.0294(6)	53.3	0.045	p-mode
f_4	29.36872(1)	0.0128(4)	73.6	29.3687(1)	0.0243(7)	49.2	0.040	p-mode
f_5	36.00084(2)	0.0074(4)	43.4	36.0010(1)	0.0240(6)	49.0	⋯	f_3+8f_{orb}
f_6	29.69563(2)	0.0073(3)	41.7	29.6954(3)	0.0148(6)	30.4	0.040	p-mode
f_7	21.87028(3)	0.0043(3)	22.0	21.8705(7)	0.0054(7)	10.0	0.054	p-mode
f_8	38.14077(8)	0.0015(4)	8.5	38.1399(8)	0.0048(6)	9.2	0.031	p-mode
f_9	4.09286(3)	0.0036(3)	18.6	4.0922(9)	0.0041(6)	6.3	⋯	$4f_8-5f_6$?
f_{10}	24.527(3)	0.0017(2)	9.8	24.53(9)	0.0034(4)	6.9	⋯	f_1-2f_2
f_{11}	2.606 98(4)	0.0033(3)	15.1	⋯	⋯	⋯	⋯	$2f_2$
f_{12}	3.775(9)	0.0025(3)	12.9	⋯	⋯	⋯	⋯	$2f_2+f_{orb}$
f_{13}	27.711(5)	0.0017(2)	8.6	⋯	⋯	⋯	⋯	f_3+f_{orb}
f_{14}	5.214 75(9)	0.0016(3)	8.4	⋯	⋯	⋯	⋯	$4f_2$

Carlo simulation in Period04, and the S/N is calculated in a box size of 2 cd^{-1} centered on the extracted frequency. All of the frequencies and LC Nyquist alias frequencies are labeled in Figure 5. The dotted red lines signify the LC Nyquist frequency labeled with f_N, and the dotted black lines indicate the 5.6σ detection thresholds.

Among these significant frequencies, we identify combinations f_i using the formula: $|f_i - (m \times f_j + n \times f_k)| < \varepsilon$, where m and n are integers between -5 and 5, f_j and f_k are independent frequencies, and ε is the Rayleigh resolution ($\varepsilon = 1.5/\Delta T$ (Loumos & Deeming 1978), $\varepsilon \approx 0.0013$ and 0.017 cd^{-1} for LC and SC data, respectively) (Pápics 2012; Kurtz et al. 2015). Since there is an orbital period threshold of $\sim$13 days below which the pulsation properties are affected by the binarity (Liakos & Niarchos 2015), the possible combinations with the orbital harmonics ($f_{orb} = 1.183\,50(3)$ cd^{-1}) are also identified. A combination is accepted if the difference is less than the Rayleigh resolution. The results are listed in the last column of Table 5.

The harmonics of f_2 ($f_{11} = 2f_2$ and $f_{14} = 4f_2$) are detected in LC data, suggesting that f_2 may be the orbital or rotational frequency (Balona 2013; McQuillan et al. 2014). Assuming that f_2 is an orbital frequency, the corresponding orbital period $P = 2/f_2 \approx 1.5342$ day. However, this period cannot match the observed RVs. Therefore, f_2 is probably due to rotation, which will be discussed in Section 4. We identify f_9 as a combination frequency with a difference slightly above the Rayleigh resolution of LC data. However, a higher combination order (order >2) will increase the probability of a chance coincidence with an independent frequency (Pápics 2012; Balona 2016). Therefore, the possibility that f_9 is a g-mode pulsation frequency cannot be ruled out. It is worth noting that f_1 shows non-sinusoidal light variability with an amplitude one order of

magnitude higher than that of other frequencies. We find that f_1 is approximately 23 times the orbital frequency, indicating that the pulsation characteristics of f_1 are possibly affected by the orbital effect.

The results from the spectral and Fourier analysis show that the primary component of KIC 10417986 matches well with the profiles of δ Scuti stars (e.g., effective temperature, luminosity and period range) (Breger 2000). Zhang et al. (2013) first deduced the theoretical relation between the pulsation and orbital period for eclipsing binaries containing δ Sct components, and suggested that the pulsation could be from p-mode if the P_{pul}/P_{orb} ratio is below 0.07. In this work, we calculate the P_{pul}/P_{orb} ratios of six independent frequencies (f_1, f_3, f_4, f_6, f_7 and f_8) with an uncertainty of 10^{-6}. All of the ratios are below 0.07. This indicates that these frequencies probably belong to p-mode pulsations. The results are listed in the last two columns of Table 5.

4. Discussion

According to the RVs and light curve analysis of KIC 10417986, the frequency f_2, which is non-sinusoidal, is probably due to rotation rather than the case of g-mode pulsation, since harmonics are generally expected at high amplitudes (Balona 2013; Kurtz et al. 2015), yet the amplitude of f_2 is only $\sim$0.03 mmag. We first check if the light variation of f_2 is caused by the ellipsoidal effect, which occurs in non-eclipsing binary stars and especially close binaries (Morris 1985; Beech 1985; Morris & Naftilan 1993), by modeling the light curves with the Fourier analysis based on the methods of Faigler & Mazeh (2011) and Faigler et al. (2012). The formula of Fourier analysis was applied to fit the light curves of
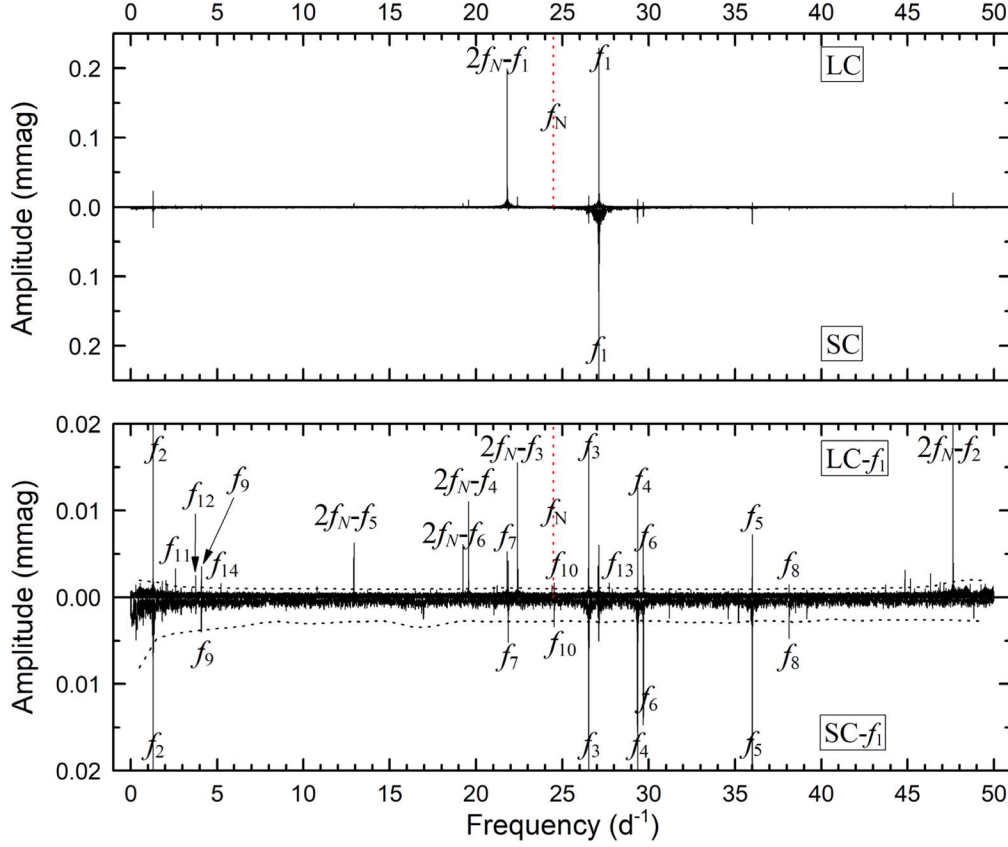
Figure 5. (Top) The Fourier amplitude spectrum of the original LC and SC light curves, in which the dominant frequency is labeled with f_1. (Bottom) The Fourier amplitude spectrum of the LC and SC light curve residuals after pre-whitening f_1, in which the frequencies except f_1 are indicated. The dotted red lines correspond to the LC Nyquist frequency labeled with f_N, and the dotted black lines indicate the 5.6σ detection thresholds of the LC and SC local noise levels.

segment 1 (see Figure 1) as follows

$$L(\theta) = A_0 + A_1 \cos(\theta) + A_2 \cos(2\theta)$$
$$+ B_1 \sin(\theta) + B_2 \sin(2\theta). \qquad (3)$$

The synthetic light curve from the Fourier models is displayed in Figure 6, and the derived Fourier coefficients are as follows: $A_0 = -0.00013980(2)$, $A_1 = -0.02802546(3)$, $A_2 = -0.00000041(3)$, $B_1 = -0.00891906(3)$ and $B_2 = 0.00013332(3)$. The results show that the $\cos(\theta)$ term is the most dominant. Thus, it is obvious that the light variation of f_2 is mainly due to the magnetic activity or other effects (e.g., reflection effect) rather than the ellipsoidal effect.

To understand the nature of f_2, we divide LC data of KIC 10417986 into four segments (see Figure 1), which have a good continuous sampling. First, all frequencies except frequency f_2 are pre-whitened from the data in each segment. Then, the residual light curves are used for the Fourier analysis. The Fourier amplitude spectrum of the residuals of each segment is displayed in the left panels of Figure 7. The second and fourth harmonics of frequency f_2 are detected in the residuals of segment 1, but only the fourth harmonic in segment 2 and
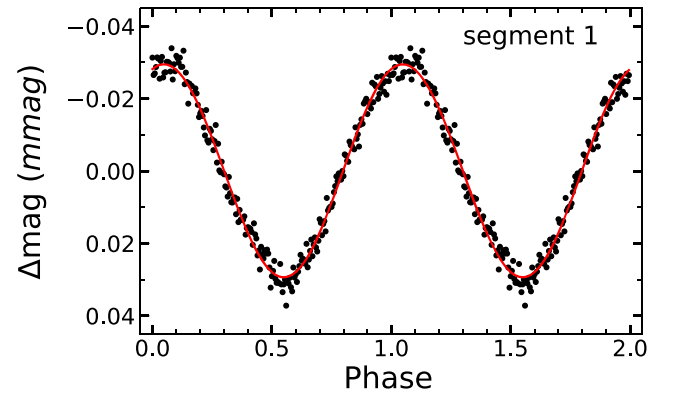
Figure 6. The observed light curve (black-filled circles) and the synthetic light curve from the Fourier models (red line) for segment 1.

segment 3, and the third harmonic in segment 4. The phase-folded light curves of f_2 for each segment are also shown in the right panels of Figure 7. Note that the data have been averaged using binning, and the number of bins is 200. It can be seen that f_2 exhibits an amplitude and phase variation over a time span of
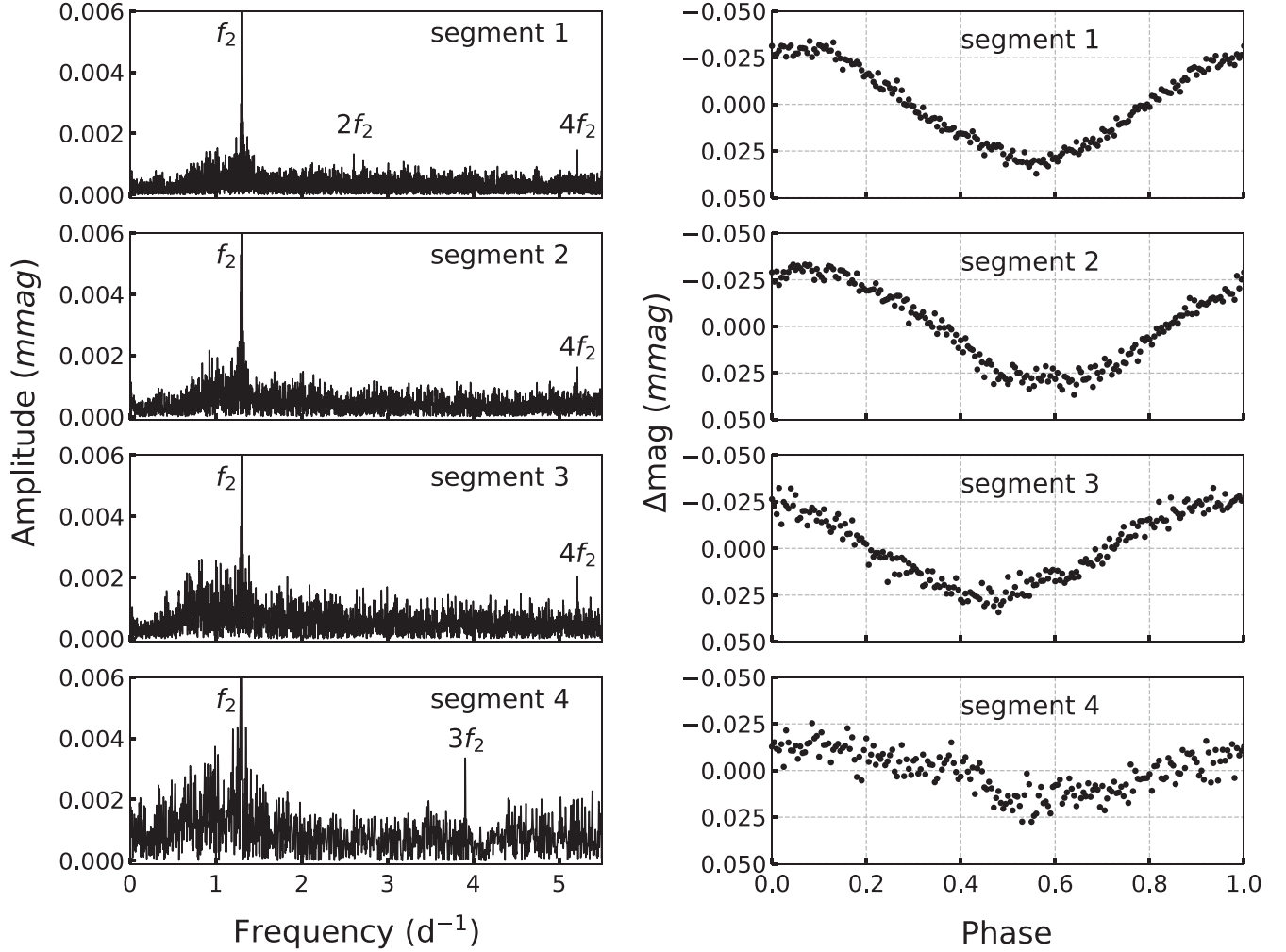
Figure 7. A comparison of the amplitude and phase of f_2 in the four segments.

about four years, indicating that the variations of f_2 are probably caused by starspots. In this case, the amplitudes of the harmonic mainly depend on the inclination of the rotation axis and the position of the spots and will sometimes be low or absent (Balona 2013). Lurie et al. (2017) found that some short-period binaries in 816 EBs with starspot modulations have rotation periods 13% slower than the orbital period, which is probably due to the surface differential rotation of starspots. However, we find the orbital period (0.84495 days) is slightly slower than the starspot rotation period ($1/f_2$= 0.76726 days). It could be the same reason but the starspots are located in the fast rotation regions (Niu et al. 2022). The surface differential rotation of stars is also found in many other works (Donahue et al. 1996; Barnes et al. 2000; Weber et al. 2005; Korhonen 2012; Özavcı et al. 2018).

According to the results of Lurie et al. (2017), binary stars with an orbital period less than 2 days are almost synchronous.

Moreover, the synchronization timescale must be shorter than the circularization timescale due to the orbit's angular momentum being generally larger than that of the stars (Zahn 1975, 2008). As KIC 10417986 is a circular orbit binary system, we propose here that the rotation period should be the orbital period of this star, 0.84495 days, and assume that $i_{rot} \approx i_{orb}$. Then, the derived equatorial rotation velocity v is about 120 km s^{-1} from the estimated radius of 2.0(1) $R_\odot$. The $v\sin i$ of 52 ± 11 km s^{-1} has been obtained from the synthetic spectral fitting. Thus, the orbital inclination i_{orb} is estimated to be $26° \pm 6°$, and subsequently, the mass of the secondary M_2 is estimated to be $0.52^{+0.18}_{-0.09}$ $M_\odot$, which is a late-K to early-M type star.

KIC 10417986 is a short-period circular orbit binary system with a semimajor axis a of about 5 $R_\odot$. We assume that the two components have not undergone material exchange. Then, the age of the system is estimated by comparing the observed
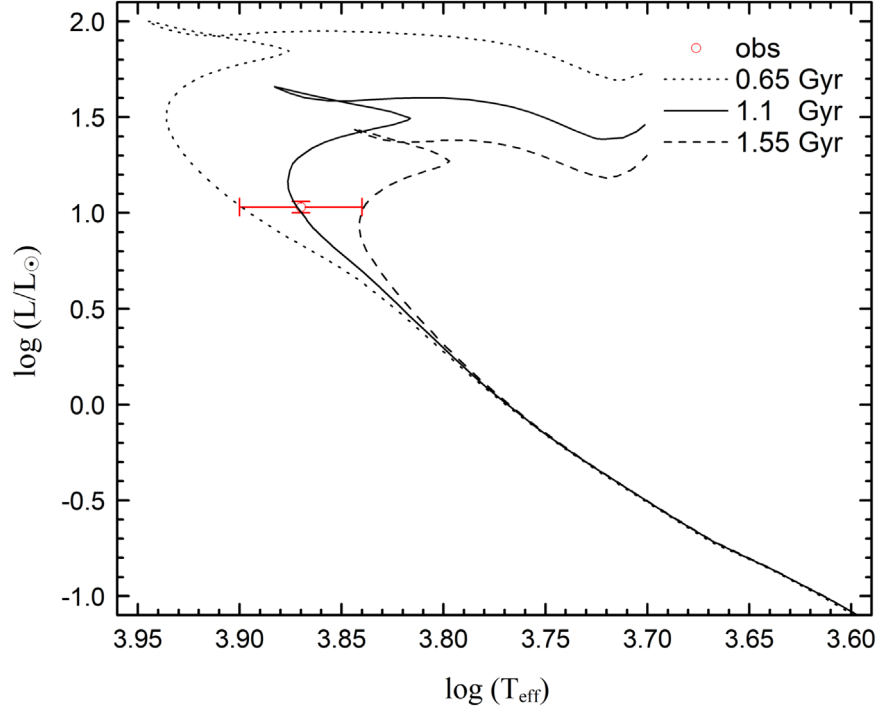
Figure 8. PARSEC isochrones for KIC 10417986 with [M/H] = 0.08 dex. The location of the primary component is labeled with a red open circle with $\pm 3\sigma$ errorbars. The dotted, solid and dashed lines are isochrones for ages of 0.65 Gyr, 1.1 Gyr and 1.55 Gyr, respectively.

temperature and luminosity of the primary with a web interface, the PAdova and TRieste Stellar Evolution Code[7] (PARSEC, version 1.2S; Bressan et al. 2012) isochrones. We use the approximation $[M/H] = \log(Z/X) - \log(Z/X)_\odot$ for PARSEC tracks, where $[M/H] = 0.08$ dex has been derived from the synthetic spectral fitting, and the present solar metal content is $Z_\odot = 0.0152$, and $Y = 0.2485 + 1.78Z$. Figure 8 depicts the location of the primary component with a $\pm 3\sigma$ credible region in the H-R diagram. Three isochrones of age = 0.65, 1.1 and 1.55 Gyr are plotted with the dotted, solid and dashed lines, respectively. The age of KIC 10417986 is estimated to be 1.1 ± 0.45 Gyr, and the primary has evolved to the late stages of the main sequence.

5. Summary

In this paper, the ground-based spectroscopic data and Kepler high-precision photometric data are combined to study the non-eclipsing binary KIC 10417986. A total of 29 single-lined spectra was observed with the 2.16 m telescope at Xinglong Station and the 1.2 m telescope at Nanshan Station. The orbital parameters of $P_{orb} = 0.844\,95 \pm 0.00002$ day, $K_1 = 29.7 \pm 1.5$ km s^{-1} and $\gamma = -18.7 \pm 1.7$ km s^{-1} are obtained by using the rvfit code, and the derived quantities are $a_1 \sin i = 0.50 \pm 0.02\,R_\odot$, $f(m_1, m_2) = 0.0023 \pm 0.0003\,M_\odot$.

The atmospheric parameters of the primary are determined by the synthetic spectral fitting technique, where $T_{eff} = 7411 \pm 187$ K and $\log g = 4.2 \pm 0.3$ dex are derived from the three combined higher resolution and 18 BFOSC lower resolution spectra, while $[M/H] = 0.08 \pm 0.09$ dex and $v \sin i = 52 \pm 11$ km s^{-1} are only from the three combined higher resolution spectra. There are 14 frequencies extracted from the Fourier analysis of LC and SC data with S/N < 5.6, of which f_2 is probably the rotational frequency due to the starspots; six independent pulsation frequencies in the high-frequency region (f_1, f_3, f_4, f_6, f_7 and f_8) probably belong to the p-mode with the P_{pul}/P_{orb} ratios below 0.07 and the rest are possibly the combinations or harmonic frequencies. From the estimated mass and radius of the primary, and the observed $v \sin i$, the derived orbital inclination is $26° \pm 6°$, and the mass of the secondary is $0.52^{+0.18}_{-0.09}\,M_\odot$, which should be a late-K to early-M type star. Finally, we estimate the age of the binary star to be about 1.1 ± 0.45 Gyr.

---

[7] http://stev.oapd.inaf.it/cgi-bin/cmd_3.4

References

Aindang, A., Inkum, R., Sarotsakulchai, T., et al. 2021, JPCS, 1719, 012017
Antoci, V., Cunha, M., Houdek, G., et al. 2014, ApJ, 796, 118
Balona, L. A. 2013, MNRAS, 431, 2240
Balona, L. A., Daszyńska-Daszkiewicz, J., & Pamyatnykh, A. A. 2015, MNRAS, 452, 3073
Balona, L. A. 2016, MNRAS, 459, 1097
Barentsen, G., Hedges, C., Vinícius, Z., et al. 2021, Zenodo, doi:10.5281/zenodo.1181928
Barnes, J. R., Collier Cameron, A., James, D. J., et al. 2000, MNRAS, 314, 162
Barros, S. C. C., Demangeon, O., & Deleuil, M. 2016, A&A, 594, A100
Beech, M. 1985, Ap&SS, 117, 69
Blanco-Cuaresma, S., Soubiran, C., Heiter, U., et al. 2014, A&A, 569, A111
Blanco-Cuaresma, S. 2019, MNRAS, 486, 2075
Breger, M. 2000, Delta Scuti and Related Stars, in ASP Conference Series, 210
Bressan, A., Marigo, P., Girardi, L., et al. 2012, MNRAS, 427, 127
Chen, X., Li, Y., & Zhang, X. 2019, ApJ, 887, 253
Chen, X., Zhang, X., Li, Y., et al. 2020, ApJ, 895, 136
Conroy, K. E., Prša, A., Stassun, K. G., et al. 2014, AJ, 147, 45
Damiani, C., Cardini, D., Maceroni, C., et al. 2010, Binaries—Key to Comprehension of the Universe, 435, 41
Donahue, R. A., Saar, S. H., & Baliunas, S. L. 1996, ApJ, 466, 384
Dotson, J., Barentsen, G., Hedges, C. L., et al. 2019, in American Astronomical Society Meeting
Eker, Z., Soydugan, F., Soydugan, E., et al. 2015, AJ, 149, 131
Faigler, S., & Mazeh, T. 2011, MNRAS, 415, 3921
Faigler, S., Mazeh, T., Quinn, S. N., et al. 2012, ApJ, 746, 185
Fan, Z., Wang, H., Jiang, X., et al. 2016, PASP, 128, 115005
Gaia Collaboration, Brown, A. G. A., Vallenari, A., et al. 2018, A&A, 616, A1
Gaulme, P., & Guzik, J. A. 2019, A&A, 630, A106
Gautschy, A., & Saio, H. 1995, ARA&A, 33, 75
Gray, R. O., & Corbally, C. J. 1994, AJ, 107, 742
Grevesse, N., & Sauval, A. J. 1998, SSRv, 85, 161
Guo, Z., Gies, D. R., Matson, R. A., et al. 2016, ApJ, 826, 69
Handler, G. 2009, Stellar Pulsation: Challenges for Theory and Observation, 1170, 403
Hestroffer, D., & Magnan, C. 1998, A&A, 333, 338
Kirk, B., Conroy, K., Prša, A., et al. 2016, AJ, 151, 68
Korhonen, H. 2012, Investigating stellar surface rotation using observations of starspots, in Proc. of the International Astronomical Union, Vol. 286, 268
Kurtz, D. W., Shibahashi, H., Murphy, S. J., et al. 2015, MNRAS, 450, 3015
Kurucz, R. L. 2005, MSAIS, 8, 14
Lenz, P., & Breger, M. 2005, CoAst, 146, 53
Iglesias-Marzoa, R., López-Morales, M., & Jesús Arévalo Morales, M. 2015, PASP, 127, 567
Liakos, A. 2020, A&A, 642, A91
Liakos, A., & Niarchos, P. 2015, Binaries with a δ Scuti Component: Results from a Long-Term Observational Survey, Updated Catalog, and Future Prospects, in Astronomical Society of the Pacific Conference Series, Vol. 496, 195
Li, Y., & Stix, M. 1994, A&A, 286, 815
Loumos, G. L., & Deeming, T. J. 1978, Ap&SS, 56, 285
Lurie, J. C., Vyhmeister, K., Hawley, S. L., et al. 2017, AJ, 154, 250
Maceroni, C., Montalbán, J., Gandolfi, D., et al. 2013, A&A, 552, A60
McQuillan, A., Mazeh, T., & Aigrain, S. 2014, ApJS, 211, 24
Morris, S. L. 1985, ApJ, 295, 143
Morris, S. L., & Naftilan, S. A. 1993, ApJ, 419, 344
Mortensen, D., Eisner, N., IJspeert, L., Kochoska, A., & Prsa, A. 2021, in AAS, 53
Murphy, S. J., Shibahashi, H., & Kurtz, D. W. 2013, MNRAS, 430, 2986
Niu, H.-B., Fu, J.-N., Wang, J.-X., et al. 2022, RAA, 22, 015016
Özavcı, I., Şenavcı, H. V., Işık, E., et al. 2018, MNRAS, 474, 5534
Pápics, P. I. 2012, AN, 333, 1053
Piskunov, N. E., Kupka, F., Ryabchikova, T. A., et al. 1995, A&AS, 112, 525
Prša, A., Batalha, N., Slawson, R. W., et al. 2011, AJ, 141, 83
Rodríguez, E., & Breger, M. 2001, A&A, 366, 178
Sarmento, P., Delgado Mena, E., Rojas-Ayala, B., et al. 2020, A&A, 636, A85
Sheminova, V. A. 2019, KPCB, 35, 129
Slawson, R. W., Prša, A., Welsh, W. F., et al. 2011, AJ, 142, 160
Stassun, K. G., Oelkers, R. J., Paegert, M., et al. 2019, AJ, 158, 138
Uytterhoeven, K., Moya, A., Grigahcène, A., et al. 2011, A&A, 534, A125
van Dokkum, P. G. 2001, PASP, 113, 1420
Videla, M., Mendez, R. A., Clavería, R. M., et al. 2022, AJ, 163, 220
Vinícius, Z., Barentsen, G., Hedges, C., et al. 2018, Zenodo, doi:10.5281/zenodo.1181929
Weber, M., Strassmeier, K. G., & Washuettl, A. 2005, AN, 326, 287
Werner, M. W., Gorjian, V., Morales, F. Y., et al. 2021, ApJS, 254, 11
Yang, T., Esamdin, A., Song, F., et al. 2018, ApJ, 863, 195
Zahn, J.-P. 1975, A&A, 41, 329
Zahn, J.-P. 2008, EAS Publications Series, 29, 67
Zhang, X. B., Luo, C. Q., & Fu, J. N. 2013, ApJ, 777, 77
Zong, P., Esamdin, A., Fu, J. N., et al. 2019, PASP, 131, 064202
Zong, W., Charpinet, S., Vauclair, G., et al. 2016, A&A, 585, A22